Radiocarbon, Vol 62, Nr 2, 2020, p 453–465 DOI:10.1017/RDC.2019.139
© 2019 by the Arizona Board of Regents on behalf of the University of Arizona

UNRAVELLING QUASI-CONTINUOUS ^{14}C PROFILES BY LASER ABLATION AMS

C Yeman[1]* • M Christl[1] • B Hattendorf[2] • L Wacker[1] • C Welte[1] • N Brehm[1] • H-A Synal[1]

[1]Laboratory of Ion Beam Physics, ETH Zurich, Otto-Stern-Weg 5, HPK, 8093 Zurich, Switzerland
[2]Laboratory of Inorganic Chemistry, ETH Zurich, Vladimir-Prelog-Weg 1-5/10, HCI, 8093 Zurich, Switzerland

ABSTRACT. Laser ablation (LA) accelerator mass spectrometry (AMS) is a novel method for rapid online radiocarbon (^{14}C) analysis of carbonates. The quasi-continuous ^{14}C profiles obtained with this technique demand a customized data evaluation protocol to relate the acquired ^{14}C data to the analyzed sample. We take into account the mixing effects due to the minimal counting (integration) time of the AMS, the finite width of the laser beam and the gas washout of the ablation volume. Thereby we mathematically describe our LA setup with a system function that acts on the produced CO/CO_2 (CO_X) from the sample resulting in a mixing of the ^{14}C profiles obtained by AMS analysis. Furthermore, we analyze the long-term target memory effect in the gas ion source and establish a routine for correction. The correction routine is tested with a stalagmite comprising a growth stop that is analyzed at different scanning velocities indicating that only the slow scanning velocity can provide the necessary resolution to determine the width of the growth stop of 365 µm.

KEYWORDS: carbonates, gas ion source, laser ablation, online ^{14}C analysis.

INTRODUCTION

Carbonates that grow over years to thousands of years, such as corals or stalagmites, are valuable archives of climate change. Radiocarbon (^{14}C) analysis of these archives in particular is used as a tracer for studying carbon cycle dynamics and paleoclimate (Genty and Massault 1997; Mangini et al. 1998). However, the ^{14}C analysis in these samples suffers from three major drawbacks. First, establishing a time series of ^{14}C requires laborious and time-consuming sample extraction by drilling and further chemical preparation for conversion to CO_2 and eventually the preparation of the graphite sample for AMS analysis. Second, the discrete sampling technique generally bears the risk of potentially overlooking valuable information between neighboring sampling points. Third, a standard AMS analysis still requires 5–10 mg of carbonate for graphitization and 0.5–1 mg of carbonate for gas measurement, which poses a strong constraint on the analysis of very small (i.e. mg-sized) samples such as otoliths (Andrews et al. 2019).

Recently, a novel online sampling and analysis method has been introduced combining laser ablation with accelerator mass spectrometry (LA-AMS) to overcome the above limitations (Welte et al. 2016a; Welte et al. 2016b). LA-AMS allows to produce spatially resolved ^{14}C profiles of carbonate records covering up to several centimeters within a few hours of measurement. Up to 5 mg of $CaCO_3$ are consumed per hour reaching a precision of 1% for modern samples. The background measured on ^{14}C free marble of $F^{14}C = 0.011 \pm 0.002$ is low and reference carbonate material is well reproduced (Welte et al. 2016b). This method is based on using a focused laser beam for the sampling of the carbonate: A pulsed laser beam with sufficient energy density can evaporate the material from the sample surface, whereby a mixture of particles and gas is produced. The gas, consisting of mainly CO, CO_2 (and O_2), can directly be flushed into an AMS system equipped with a gas ion source (Ruff et al. 2007; Synal et al. 2007). By constantly moving the sample under the laser, a continuous carbon flow is guaranteed. The AMS data acquisition, however, has a minimum integration time leading to a quasi-continuous ^{14}C profile. This means that a single data point always represents a certain spatial range on the sample that is given by the integration time and the velocity at which the sample is moved under the laser.

*Corresponding author. Email: yemanc@phys.ethz.ch.

https://doi.org/10.1017/RDC.2019.139 Published online by Cambridge University Press

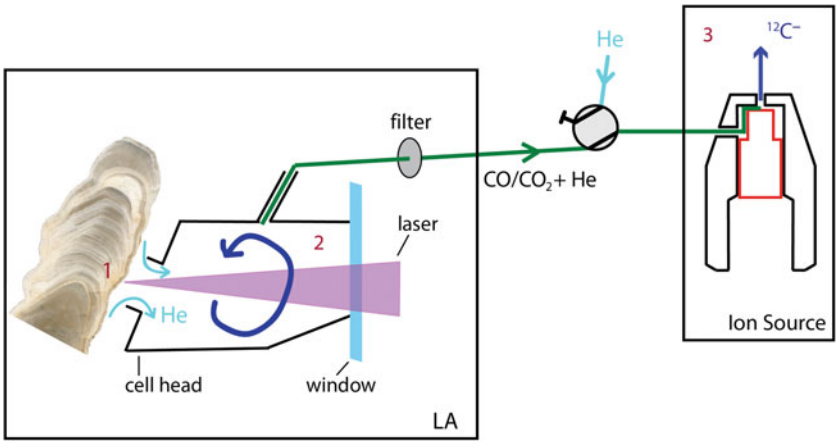

Figure 1 Schematic view of the LA-AMS system. CO and CO_2 are produced by LA in the ablation volume (left box) and then transported via a glass capillary to the ion source of the AMS (right box) passing two consecutive filters. A valve allows switching between the cell head and a He line for flushing the capillary to the ion source. The mixing effects are marked with red numbers: 1—laser-beam width, 2—washout, 3—target memory. (Please see electronic version for color figures).

While LA AMS offers great advantages in producing highly resolved ^{14}C records, the data evaluation involved with this approach needs careful considerations as during the measurement quasi-continuous ^{14}C profiles are produced rather than distinct point estimates (e.g. from a micro-drilled carbonate sample). The main effects considered here are (numbers in Figure 1):

1. **Laser-beam width.** When combining several AMS data points (typically provided as 10 s averages over the continuous analysis) neighboring subsamples overlap spatially with a width that is equal to the laser width d_L.
2. **Washout.** The gas produced by a laser pulse mixes with that of preceding and subsequent pulses. Consequently, a delayed and smoothened $^{14}C/^{12}C$ ratio is determined in the AMS.
3. **Target memory.** Since the start of gas ion source AMS in the 1980s the problem of a target memory is known (Bronk Ramsey and Hedges 1987). While for the standard ^{14}C AMS analysis (gas or graphite) one AMS target is assigned to a single sample with a given (constant) ^{14}C concentration, during LA-AMS a continuous flow with changing ^{14}C concentration is produced and measured using the same AMS gas target. This means that gas target memory effects have to be considered.

The aim of this work is to present and discuss these three main effects and to develop a new data reduction strategy optimized for LA-AMS.

MATERIAL AND METHODS

Instrumental Setup

Since 2014, the LA interface connected to the gas ion source of the MICADAS at ETH (Synal et al. 2007; Wacker et al. 2010a) has been in use for online ^{14}C analysis of carbonates (Welte et al. 2016a, Welte et al. 2016b). A pulsed ArF excimer laser (193 nm,

https://doi.org/10.1017/RDC.2019.139 Published online by Cambridge University Press

Table 1 Key factors for carbon production.

Fluence on sample surface.	1–23 J/cm^2
Laser repetition rate	150–250 Hz
Ablation rate $CaCO_3$	50–90 µg/min
Velocity of sample	5–500 µm/s

8 ns pulse duration, GAM LASER, Orlando, USA) is focused onto the plane surface of the sample. The LA-AMS setup used in this study was modified from the version described in (Welte et al. 2016a, 2016b). This comprises that the rectangular spot size of the laser was reduced from 110 × 680 µm^2 to 75 × 140 µm^2. Furthermore, the fluence on the sample surface was increased, which leads to a higher ablation rate and gaseous carbon production (Welte et al. 2017), resulting in a similar carbon flow rate while reaching higher spatial resolution. To move the sample under the laser, it is fixed in a holder that is mounted on an x-y positioning system in a box of two compartments (sample box). The big compartment has a volume of about 700 mL, typically filled with 200–500 mbar He that acts as a carrier gas and contains the positioning system. The small compartment is the ablation volume where the ablation process takes place, shown in Figure 1 (LA box) with a size of 900 µL (modified). For online AMS analysis, only the gaseous proportion of the ablated material is suitable. Exiting the cell, the ablated material passes through two consecutive frits with pore sizes of 2 µm and 0.5 µm (Valco frits, Vici International AG), respectively. The remaining gas mixture of He carrier gas and CO_X and O_2 is then transported into the ion source of the MICADAS via a fused silica capillary (Ø 220 µm, l = 1 m). This gas flow is restricted to less than 3 mL/min to guarantee high vacuum conditions in the ion source. Gas targets used for LA-AMS are the same as for standard gas measurements (Ruff et al. 2007; Fahrni et al. 2013).

The key parameters influencing the gaseous C production of roughly 6 µg/min are the fluence and frequency of the laser pulse as well as the velocity of the sample moving under the laser (see Table 1). The depth of the laser track is 250 µm at a speed of 10 µm/s and repetition rate of 200 Hz. Even at a minimum speed of 5 µm/s the carbon production is constant, and no signal is lost due to crater depth. Redeposited material is negligible compared to the ablated sample volume.

Measurement Sequence

The existing LA-AMS setup is in operation at three scanning modes (Welte et al. 2016a)—layer scan, precision scan, and survey scan. With the layer scan, the laser is ideally moving along the growth layers constantly producing a gas mixture of one $^{14}C/^{12}C$ ratio. This mode is most similar to a regular AMS gas measurement. The precision scan describes a zigzag pattern where the laser scans up and down within growth layers while slowly moving forward across layers of different years of formation indicated by a small displacement dx. This extends the measurement time while crossing only very few growth layers, which increases counting statistics and therefore leads to more precise results. In the third scanning mode, the survey scan, the sample is ideally moved parallel to the growth axis. In the following, only survey scans will be discussed with regard to data evaluation because only in this case the $^{14}C/^{12}C$ ratio of the ablated sample material is expected to change continuously with measurement time.

https://doi.org/10.1017/RDC.2019.139 Published online by Cambridge University Press

LA-AMS measurements follow a standard procedure: First, the ion source of the AMS is tuned using a CO_2 gas standard fed into the gas interface system (Ruff et al. 2007; Wacker et al. 2013). The measurement sequence then starts with the analysis of a CO_2 gas standard (5% CO_2 in helium from NIST Ox-II standard) and a gas blank (5% CO_2 in helium, Messer Schweiz AG, Lenzburg, Switzerland). Both measurements are later used for blank subtraction and normalization, respectively, following BATS data reduction (Wacker et al. 2010b). Next, the LA system is connected to the ion source and a carbonate blank and reference carbonate material are measured to affirm operational quality of the LA-AMS setup (Welte et al. 2016b). After this setup procedure the LA AMS measurements of the unknown samples start. In between samples, the carbonate blank and reference are repeatedly measured as quality and drift control. After each LA AMS sample the cell is evacuated and filled with pure helium gas to minimize crosstalk between consecutive samples. This cell cleaning procedure is repeated three times.

At the MICADAS AMS system, ^{14}C atoms are counted for a minimum time of $t_C = 10$ s, which is referred to as one cycle. During one cycle, the sample is moved between 50 and 5000 µm under the laser (velocities given in Table 1). Consequently, the measured $^{14}C/^{12}C$ ratio is always a mixture of $^{14}C/^{12}C$ ratios of the ablated material within one single cycle ultimately defining the limit of the spatial resolution. A single gas target can be used for up to about 100 cycles and such a measurement on one gas target is referred to as a run. Usually several runs are necessary to record the complete ^{14}C record of one sample (coral, stalagmite, etc.), which is usually reported in $F^{14}C$ representing the blank, background, and fractionation corrected $^{14}C/^{12}C$ ratio relative to a standard (Reimer et al. 2004).

A LA-AMS run starts with pre-sputtering the gas target for a few cycles with only helium flowing into the ion source to flush the capillary and clean the target surface. Then, the laser and the sample positioner are switched on and the sample starts moving at a predefined, constant velocity v_S. At the same time, the gas flow path is connecting the sample box with the ion source and the carbon current rises (Figure 2A). The first two cycles of rising currents are extrapolated (see red line in Figure 2A) to obtain the intercept $t_0 = t(x = 0)$ with the measurement time axis, which is correlated to the starting position x_0 of the laser. From x_0 on with every cycle the distance $dx = t_C \cdot v_S + d_L$ is covered by the laser on the sample.

MIXING PROCESSES IN LA AMS

Overlap Due to Laser-beam Width

During a survey (or zigzag) scan in LA-AMS, the AMS records a temporal $^{14}C/^{12}C$ signal in single cycle steps of 10s while the sample is moved continuously under the laser at a velocity v_s. Due to the finite width of the laser spot the $^{14}C/^{12}C$ signal recorded during two consecutive cycles always contains a spatial overlap (Figure 2B). In this section, a closer look on how to reprocess the AMS data is taken in order to disentangle the overlapping signal.

With every laser pulse, an integral $^{14}C/^{12}C$ ratio from the area covered by the laser spot is produced. During a scan, the time that each location on the sample is ablated can be expressed with: $t_L = \frac{d_L}{v_S}$, where d_L is the width of the laser-beam spot and v_S the velocity with which the sample is moved under the laser. When starting the laser, the sample simultaneously starts moving, which leads to a linear increase of depth in the cross section

https://doi.org/10.1017/RDC.2019.139 Published online by Cambridge University Press

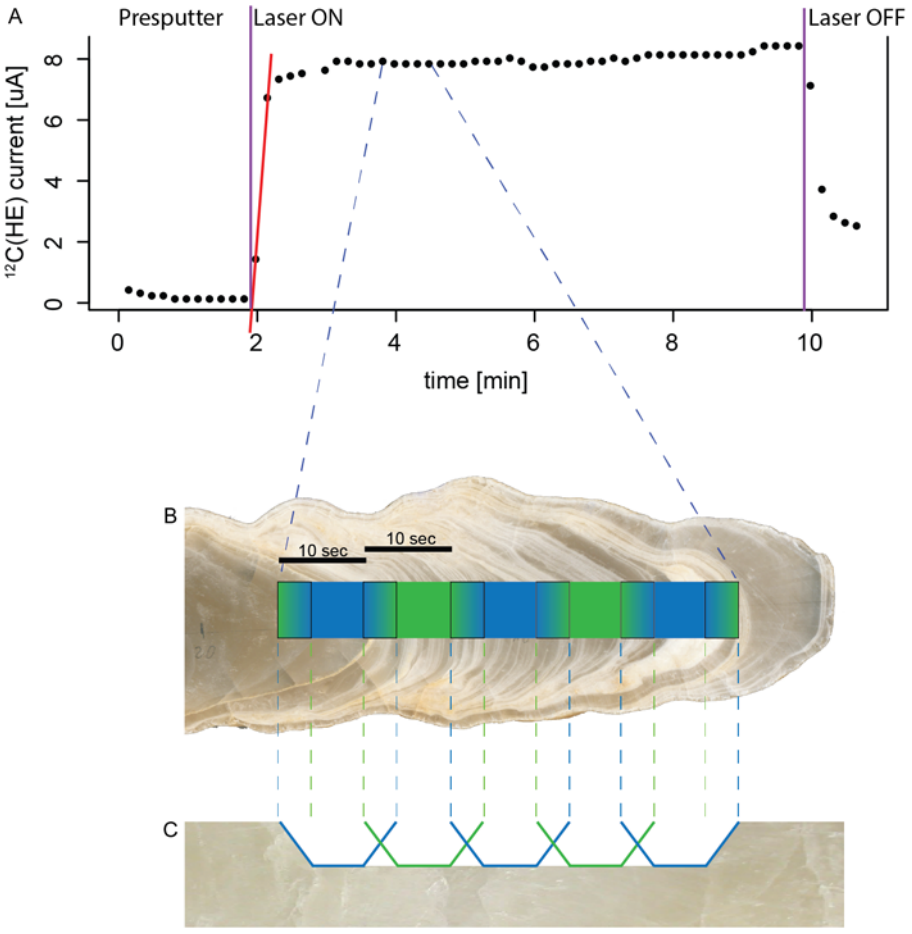

Figure 2 A—^{12}C current of a typical LA AMS measurement with rise of the current when the laser is turned on and drop in the current when the laser is turned off. B—zoom into 5 cycles to show schematically the movement of the laser-beam spot on the sample. The black rectangles indicate the area of the overlap which is the size of the laser-beam spot. The colors imply that material from this area contributes to two cycles. C—depth profile on the sample; colors show contribution to the respective cycles.

at the beginning of the scan (see Figure 2C). At the end of the full scan, this is likewise true but in reversed direction. Additionally, at the end and start of each cycle an area corresponding to the laser-beam spot size (black rectangles in Figure 2B) contributes to two consecutive cycles, indicated by the color gradient in Figure 2B. The cross section illustrates the proportion at each location that contributes to neighboring cycles. The area of the overlap compared to the overall area covered within one cycle depends on the scanning velocity: $\frac{d_L}{v_S \cdot t_C + d_L}$. The overlap decreases with higher velocities but so does the spatial resolution. To ensure both, good counting statistics and high spatial resolution it is beneficial to select low scanning velocities down to 5 µm/s (see application). During offline data analysis, the number of cycles that are integrated can be chosen in order to minimize the effect of the overlap and to improve counting statistics while ensuring high spatial resolution by selecting slow scanning velocities.

https://doi.org/10.1017/RDC.2019.139 Published online by Cambridge University Press

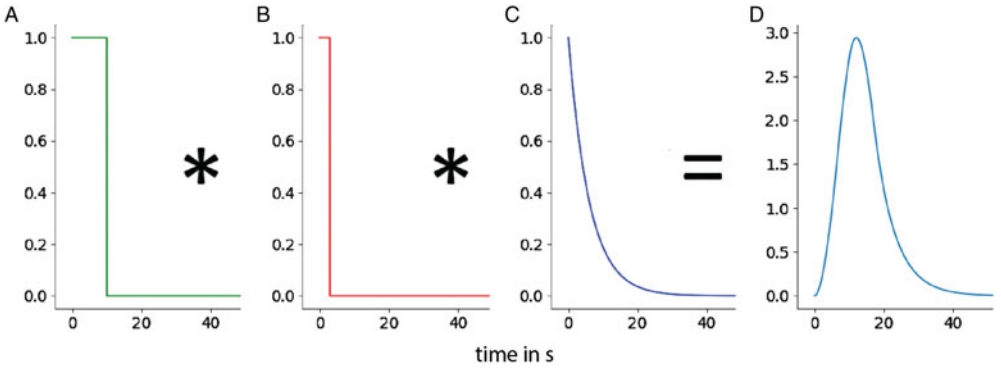

Figure 3 Functions describing A—minimum counting time, B—overlap due to laser-beam width, C—cell washout and short-term target memory, and D—system function. The convolution is implicated by "*" following Eq. (2).

Cell Washout

The modified ablation volume of the LA setup is V = 900 µL with an optimized He working pressure of 200–500 mbar. The produced CO_X mixes within this volume before it is transported into the ion source with a He carrier gas flow of typically 1.5 mL/min. Additionally, gas from the ablation volume leaks into the sample box. Welte et al. (2017) estimated that while CO_X is produced at a rate of 6 µgC/min, only 2–3 µgC/min actually reaches the ion source. As a result, the ablation volume is flushed with a flow rate of about 3 mL/min, of which half goes to the ion source and the other half leaks into the sample box (Welte et al. 2017). The produced CO_X is mixed in the ablation volume and transported into the ion source where it is additionally mixed due to the short-term memory effect of the gas target (see section target memory). The washout time constant of these processes was determined experimentally to be $\tau = 6$ s by stopping the laser and therefore the carbon production and measuring the decline in the $^{12}C^-$ current (Welte et al. 2016b). Thus, the CO_X produced by each laser pulse ($C_n(t)$) follows (Bleiner et al. 2005):

$$C_n(t) = C_{0,n} e^{-\lambda_w (t - t_0)} \tag{1}$$

At t_0 the laser produces a certain amount of CO_X (C_0) that is washed out of the cell and sputtered off the target with a "decay constant" $\lambda_w = 1/\tau$ (shown in Figure 3C).

System Function

From ablation spot to the ion source, the initial $^{14}C/^{12}C$ ratio ablated by every laser pulse is delayed and mixed by the LA AMS system. The three mixing processes (Figure 3A–C) discussed above cause a convolution of the final signal, and hence can be summarized in one system function g (Eq. 2 and Figure 3D): (1) $c(t_c)$ represents the minimum counting time $t_c = 10$s, (2) $l(t_L)$ describes the overlap with $t_L = \frac{d_L}{v_S}$ and (3) $w(\lambda_w)$ indicates the washout of the ablation volume as well as the short term target memory ($\lambda_w = 1/6\ s^{-1}$):

$$g = c(t_C) * l(t_L) * w(\lambda_w) \tag{2}$$

The constant system function (Figure 3D) describes the response of the LA-AMS setup for this given set of operational parameters. If one of the parameters changes, the system function is

https://doi.org/10.1017/RDC.2019.139 Published online by Cambridge University Press

updated accordingly. The long term target memory effect would constantly modify the system function and therefore cannot be included here. It will be discussed in the following section.

Target Memory

Model for Target Memory

The gas produced by LA contains CO_X, which is directed onto the titanium surface of the AMS gas target. The carbon is partially adsorbed by titanium and then sputtered by the Cs beam. At the same time a proportion of the carbon ions is implanted into the titanium (Stout and Gibbons 1955; Vlasyuk et al. 1986). For our model, we describe the carbon fixed on the target with two reservoirs, where carbon is deposited respectively released at different (long and short) timescales.

The reservoir with the short time constant represents carbon that is deposited on and rapidly removed from the inner, main sputtering region of the gas target. This short-term target memory effect is conceptually indistinguishable from the cell washout, and its time constant is already included in λ_w (Eq. 2).

The reservoir with the long time constant is assumed to represent the carbon deposited on and removed from the outer (halo) part of the Cs sputtering region. The time constant λ_L of this process is significantly longer compared to the minimum counting time of the AMS, which leads to a memory effect that increases with time. The temporal evolution of this long-term target memory can be described by:

$$\frac{dA(t)}{dt} = -\lambda_L \cdot A(t) + P \tag{3}$$

With P describing the constant carbon deposition rate on the halo sputter region of the target and $A(t)$ representing the released carbon from the outer halo part relative to the total sputtered carbon.

The total C^- current from the ion source I is the sum of (1) the ion current from the incoming sample gas (I_S) that underwent all previously described mixing processes (i.e. laser width, cell mixing, and the short term target memory) and (2) the current (I_T) from the above described long term target memory effect.

$$I = I_S + I_T = (1 - A(t)) \cdot I + A(t) \cdot I \tag{4}$$

Experimental Validation and Determination of Time Constants for the Target Memory Model

Both, the evolution of $A(t)$ and the time constant for the long-term memory effect have to be determined experimentally. Therefore, measurements were performed using the gas interface system (GIS) without LA cell. Hence, mixing effects in the LA setup were avoided and the long-term target memory could be studied exclusively. With the GIS the carbon flow into the ion source can precisely be controlled ensuring equal conditions for all measurements on different targets.

In Figure 4A the temporal evolution of the ion currents measured on four gas targets over 20, 40, 60, and 80 cycles is shown. First, the target is pre-sputtered, then the gas is introduced at a carbon flow of 2.2 µg/min and after the respective amount of cycles (at time $t = t_{off}$) the

https://doi.org/10.1017/RDC.2019.139 Published online by Cambridge University Press

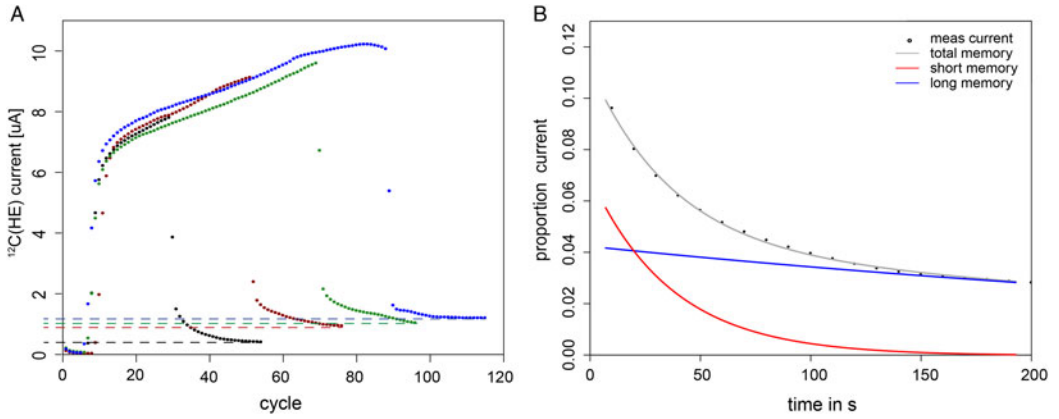

Figure 4 A—^{12}C ion current on the high energy side from four different targets at same carbon flow from GIS into the ion source. Carbon flow was stopped after counting times of 20, 40, 60, 80 cycles; B—zoom into the drop of ^{12}C current of the black curve in A. The decline follows two exponential function with long and short time constant.

capillary to the ion source is shut stopping the gas flow into the ion source. This leads to an immediate drop in the ion current caused by the emptying of the capillary, which then continues to decrease slowly indicating the contribution of the long-term target memory. The dashed lines in Figure 4A mark the ion current level determined 25 cycles after each t_{off} clearly showing that the long-term target memory increases with measurement time. Without the gas in the ion source the ionization and negative ion extraction efficiency increases by roughly 100% (supplementary information). To compare the remaining current with its contribution under gas condition the ion current is halved.

Using the above described model for the target memory, the temporal evolution of the ion current from the gas target after t_{off} is described by two exponential functions with short (λ_S) and long (λ_L)-time constants, respectively.

$$I_{meas}(t > t_{off}) = I_{meas}(t_{off}) \cdot ((1 - A(t_{off})) \cdot e^{-\lambda_S t} + A(t_{off}) \cdot e^{-\lambda_L t}) \quad (5)$$

Consequently, two exponential decay functions are fitted to the data (red and blue curves in Figure 4B). The observed behavior of the measured data matches well with the sum of the two curves ("total memory" in Figure 4B) indicating that the two-compartment model is sufficient to describe the target memory adequately. The fitted time constant from the four targets (Figure 4A) for the long-term memory is $\lambda_L = (1.7 \pm 0.2) \cdot 10^{-3} s^{-1}$ corresponding to a time constant τ_L~600 s. With measurement durations up to 100 cycles (1000s), the long-term target memory continuously increases without reaching equilibrium (compare Figure 4A). Hence, the parameters λ_L, and P to describe and correct for the long-term target memory have to be considered. However, in the LA-AMS setup the short-term target memory is already included in the washout function as discussed before.

CORRECTION PROCEDURE AND APPLICATION

Based on the above results, a dedicated correction procedure for LA AMS measurements was developed. The initial aim was to first correct the data for the long-term target memory and subsequently deconvolve it using the system function described previously. In reality, the

https://doi.org/10.1017/RDC.2019.139 Published online by Cambridge University Press

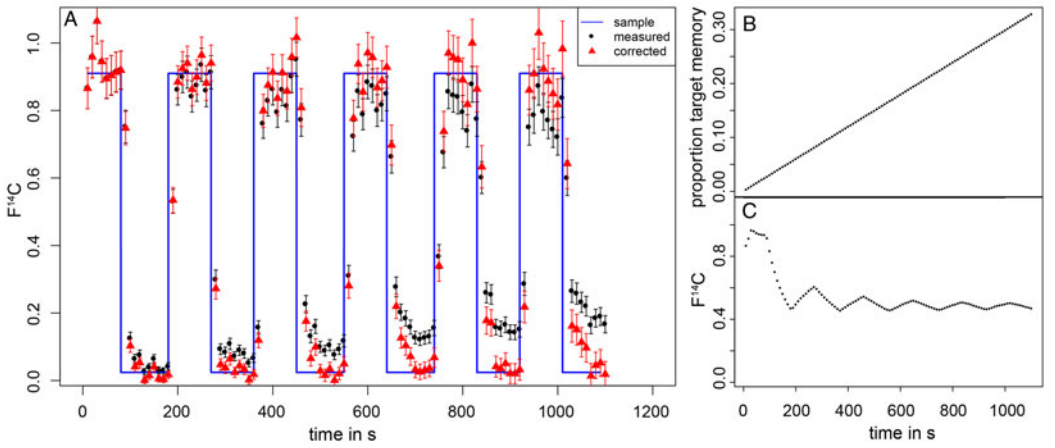

Figure 5 A—rectangular function (blue) measured with LA AMS (black). Parameters are fitted so after target memory correction the measured data yield the sample value (red). B—build-up of target memory, C—evolution of $F^{14}C$ on target.

measured data contains a finite level of noise, e.g. due to counting statistics of the AMS, which is amplified during deconvolution compromising this data correction approach. Even though in theory noise can be included in the system function if it is constant and a characteristic noise sample is available (Xiaodan et al. 2016), in the case of LA-AMS, the noise level depends on the $^{14}C/^{12}C$ ratio of the sample preventing a general description of noise to be included in the system function. In cases of rapid and large (i.e. step like) $^{14}C/^{12}C$ signal changes in a sample, e.g. due to the presence of the bomb peak, the system function still can be used to determine the timing and duration of the signal change. A two-step process is chosen for such cases: first, the parameters of both, the system function and long-term target memory are experimentally determined by analyzing a sequence of samples with known and alternating $^{14}C/^{12}C$ ratios (Figure 5A). Then, the position and duration of a step like $^{14}C/^{12}C$ change in an unknown sample can be determined (1) by correcting for the long-term target memory and (2) by fitting a step function to the data that has been convolved with the experimentally determined system function. At the start of every measurement day, this rectangular function has to be determined in order to assess the actual parameters for correction.

Design of the Experiment

Two carbonate materials with well-known but significantly different $^{14}C/^{12}C$ ratios (marble $F^{14}C = 0$ and a modern sample $F^{14}C = 0.9$) were positioned closely side by side. In order to create an ideal rectangular signal function, first one sample is ablated with a comparably slow lateral velocity of $v_S = 10\,\mu m/s$ followed by a quick movement (2000 µm/s) to the next sample while material is continuously being ablated. This sequence is repeated several times as shown in Figure 5A, where the effect of the long-term target memory causing the modern sample to appear increasingly older and vice versa can clearly be observed. We note that the precision decreases with time, which is caused by declining ion currents during the measurement. This effect is quite common in gas-AMS because of the accumulation of carbon on the gas target (Fahrni et al. 2013). However, during this experiment the measurement time was twice as long as for a normal gas AMS measurement

https://doi.org/10.1017/RDC.2019.139 Published online by Cambridge University Press

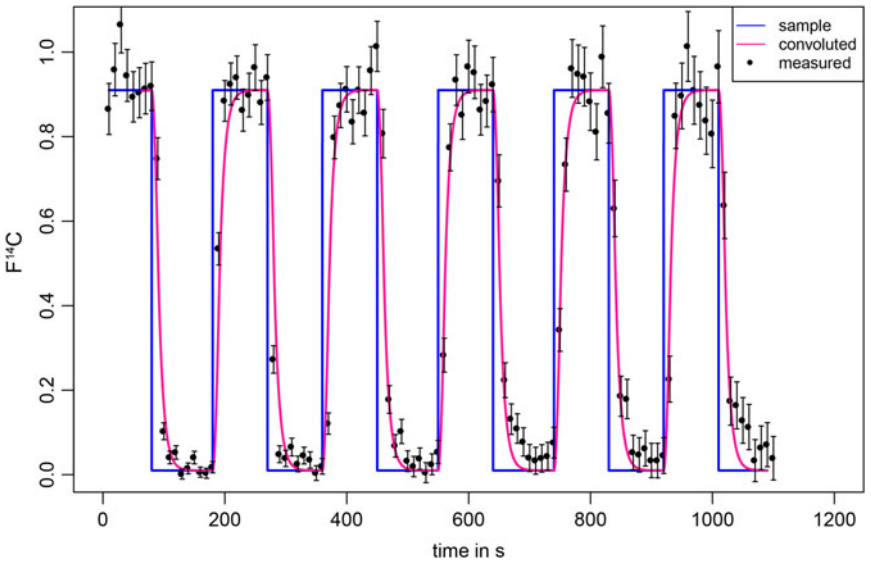

Figure 6 In pink the convolution of rectangular function (blue) with the system function and fitted to the long-term target memory corrected data (black).

and therefore the effect of decreasing precision is exaggerated (Figures 5A and 6). From the comparison of the recorded signal (black dots in Figure 5A) with the ideal rectangular function (blue line in Figure 5A) all necessary correction parameters can be determined.

Determination of Long-Term Target Memory

To correct the long-term target memory, the time evolution of the proportion of the long-term target memory (A(t)) and the corresponding $^{14}C/^{12}C$ variation ($F^{14}C_T(t)$) are determined. Using Eq. (3) an iterative approach is chosen to determine the parameters P and λ_L.

Starting with $A(t=0)=0$, $A(t+1)$ is calculated as (see Figure 5B):

$$A(t+1) = A(t) + dA = A(t) - \lambda_L \cdot A(t) \cdot dt + P \cdot dt \tag{6}$$

With dt representing the 10 s minimum integration time of the AMS. Then, the evolution of $F^{14}C_T(t)$ (Figure 5c) of the target memory is calculated:

$$F^{14}C_T(t+1) = ((A(t) - \lambda_L \cdot A(t)) \cdot F^{14}C_T(t) + P \cdot F^{14}C_{meas}(t+1))/A(t+1) \tag{7}$$

Finally, the corrected $^{14}C/^{12}C$ data ($F^{14}C_{S,T}(t)$) is calculated (red triangles in Figure 5a):

$$F^{14}C_{S,T}(t+1) = (F^{14}C_{meas}(t+1) - F^{14}C_T(t) \cdot A(t))/(1 - A(t)) \tag{8}$$

By comparing the corrected $^{14}C/^{12}C$ ratios with the measured data using a minimized χ^2 approach, the parameters P and λ_L are obtained. In the above example the fitted parameters are $P = 3{\cdot}10^{-4}s^{-1}$ ($\sigma < 10\,\%$) and $\lambda_L = 0$. These values are used to correct the measured $^{14}C/^{12}C$ ratios for the long-term target memory (red triangles in Figure 5A). The fact that λ_L approaches zero in this case indicates

https://doi.org/10.1017/RDC.2019.139 Published online by Cambridge University Press

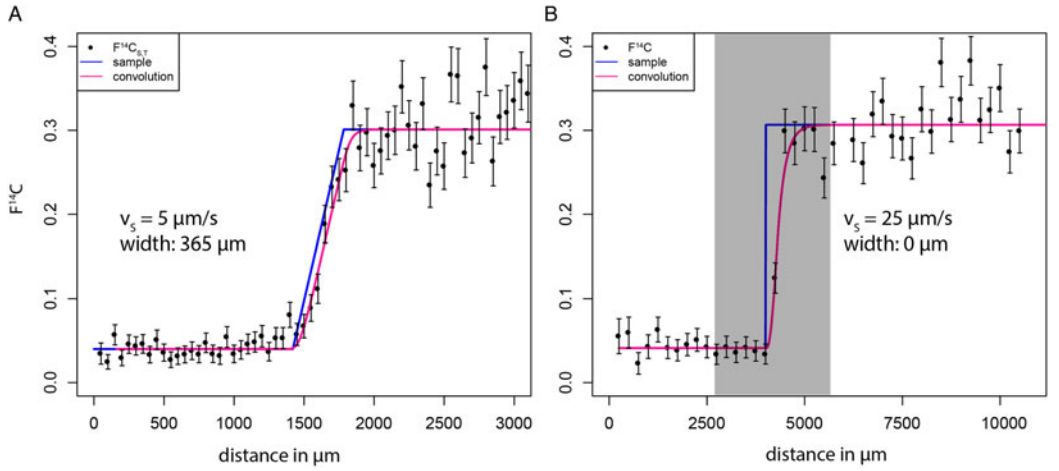

Figure 7 Growth stop in a stalagmite measured with different velocities and scanning directions in black, in blue the idealized $F^{14}C$ of the sample, and in pink its convolution with the system function. The grey area in B is the equivalent distance covered in A.

that the relative contribution of the long-term target memory linearly increases at least over the time range of about 20 min. Every measurement day the parameters P and λ_L have to be determined anew due to varying measurement conditions.

Determination of Washout and Short-Term Target Memory

The time constant for the cell washout and the short-term target memory ($1/\lambda_W$) are determined by comparing the measured and long-term target memory corrected data ($F^{14}C_{S,T}(t)$) with the rectangular function (blue line in Figures 5a and 6). $F^{14}C_{S,T}(t)$ is a result of a convolution of the system function (g) with the idealized rectangular function (s). Because the direct deconvolution of $F^{14}C_{S,T}(t)$ is impeded by the presence of noise, the original data is reconstructed by fitting the system function (g), using λ_W as fitting parameter, so that the convolution of the system function (g) with the true sample signal (s) agrees with the long-term memory corrected data (Figure 6).

The best fit is shown in pink in Figure 6a, with $\lambda_W = 0.13\ s^{-1}$. Hence the washout time constant of our system is $\tau_W \sim 8s$. This is similar to previous estimates of the washout time of the original setup (Welte et al. 2017).

Application to a Stalagmite Record

The potential of a known system function is demonstrated by the measurement of a speleothem with intermediate growth stop. There is multiple evidence for a hiatus in the stalagmite record (Welte et al. 2017). It is, however, not clear whether this was an abrupt growth stop or a gradual ceasing of carbonate accretion. To solve this question, the ^{14}C record of the stalagmite is determined with LA AMS and the above correction procedure is applied to calculate the spatial extent of the growth stop.

The LA AMS measurement with $v_S = 5$ µm/s reveals a quick rise from $F^{14}C = 0.05$ to $F^{14}C = 0.29$ (Figure 7A). Looking at the raw data, the rise covers approximately 10 data

https://doi.org/10.1017/RDC.2019.139 Published online by Cambridge University Press

points (10 s each), which translates in a spatial extent of the growth stop of about 575 µm (10 cycles + laser-beam width). This certainly is an overestimation of the length of the growth stop because of the described mixing processes. To correct for these processes, first, the long-term target memory is corrected using the parameters discussed herein, and subsequently the complete system function (Eq. 2) is used (with the known parameters t_C, t_L, and λ_w) to determine a more realistic estimate of the length of the growth stop. Starting with an ideal step function (width = 0 µm) the convolved signal is calculated. Based on a χ^2 fit the start of the rise and the width of the step function are optimized (blue line in Figure 7). The best fit of the convolved signal (pink curve in Figure 7) to the data in this first case is obtained with a width of the step function of 365 µm. This procedure was also applied to the same stalagmite record using a laser scanning velocity of 25 µm/s. The width derived from the measurement at 5 µm/s is 365 µm (Figure 7A), which is shorter than the initially estimated width of 575 µm. This shows that the correction procedure enables a more precise and robust determination of the start and the duration of the growth stop. In case of the fast scanning velocity of 25 µm/s, the laser crosses the step like signal in less than two cycles, which is too fast to resolve the step width. As a result, the growth stop appears as an ideal step with zero width (see Figure 7B and D) implying that the minimal achievable resolution is defined by the distance covered by the laser during two measurement cycles (20 sec). Using this practical estimate of the spatial resolution, structures with about 175 µm (two cycles + laser-beam width) can be resolved with the slow scanning velocity, while only 575 µm are reached with the fast scanning velocity.

CONCLUSION

For the spatially highly resolved ^{14}C analysis of carbonates by Laser Ablation AMS a new approach for data handling was developed. The main processes causing mixing and delay of the signal were described. The minimum counting time of the AMS, the finite laser-beam width, the washout of the ablation cell and the short-term memory of the target are constant processes within one measurement and therefore summarized to one system function. The long-term target memory is a slow process building up due to adsorption of carbon on the target. To determine the parameters for long-term target memory correction and the system function an artificial rectangular function put together by two samples of high and low $^{14}C/^{12}C$ ratios is analyzed. As a result, we estimated the washout time constant to be ~ 8 s. Lastly, with a complete system function, rapid changes are located on the sample more precisely, as demonstrated by measuring a growth stop in a stalagmite. Only the slow scanning velocity can provide the necessary resolution to determine the width of the growth stop of 365 µm. This method is also applicable for determining the position and duration of rapid, high magnitude changes of the ^{14}C signal such as the ^{14}C bomb pulse. It will be implemented in routine data analysis of such records produced with LA-AMS.

ACKNOWLEDGMENTS

Financial support was given by SNF (project 160064) and is gratefully acknowledged. We thank Anton Vaks for providing the stalagmite sample material from Okhotnichya Cave. Many thanks to the anonymous reviewers for their insightful comments that helped to improve this manuscript.

https://doi.org/10.1017/RDC.2019.139 Published online by Cambridge University Press

SUPPLEMENTARY MATERIAL

To view supplementary material for this article, please visit https://doi.org/10.1017/RDC.2019.139

REFERENCES

Andrews AH, Yeman C, Welte C, Hattendorf B, Wacker L, Christl M. 2019. Laser ablation–accelerator mass spectrometry reveals complete bomb ^{14}C signal in an otolith with confirmation of 60-year longevity for red snapper (*Lutjanus campechanus*). Marine and Freshwater Research. doi: 10.1071/MF18265.

Bleiner D, Belloni F, Doria D, Lorusso A, Nassisi V. 2005. Overcoming pulse mixing and signal tailing in laser ablation inductively coupled plasma mass spectrometry depth profiling. Journal of Analytical Atomic Spectrometry 20(12):1337–1343.

Bronk Ramsey C, Hedges REM. 1987. A gas ion source for radiocarbon dating. Nuclear Instruments and Methods in Physics Research B 29(1):45–49.

Fahrni SM, Wacker L, Synal H-A, Szidat S. 2013. Improving a gas ion source for ^{14}C AMS. Nuclear Instruments and Methods in Physics Research B 294:320–327.

Genty D, Massault M. 1997. Bomb ^{14}C recorded in laminated speleothems: Calculation of dead carbon proportion. Radiocarbon 39(1):33–48.

Mangini A, Lomitschka M, Eichstädter R, Frank N, Vogler S, Bonani G, Hajdas I, Patzold J. 1998. Coral provides way to age deep water. Nature 392(6674):347–348.

Reimer PJ, Brown TA, Reimer RW. 2004. Discussion: Reporting and calibration of post-bomb ^{14}C data. Radiocarbon 46(3):1299–1304.

Ruff M, Wacker L, Gäggeler HW, Suter M, Synal H-A, Szidat S. 2007. A gas ion source for radiocarbon measurements at 200 kV. Radiocarbon 49(2):307–314.

Stout VL, Gibbons MD. 1955. Gettering of gas by titanium. Journal of Applied Physics 26(12): 1488–1492.

Synal H-A, Stocker M, Suter M. 2007. MICADAS: A new compact radiocarbon AMS system. Nuclear Instruments and Methods in Physics Research B 259(1):7–13.

Vlasyuk RZ, Kurovskij VY, Lyapunov VP, Radomysel'skij ID. 1986. Interaction of titanium and vanadium with carbon dioxide under heating. Poroshkovaya Metallurgiya (Kiev) 25(1): 54–57.

Wacker L, Bonani G, Friedrich M, Hajdas I, Kromer B, Němec M, Ruff M, Suter M, Synal H-A, Vockenhuber C. 2010a. MICADAS: Routine and high-precision radiocarbon dating. Radiocarbon 52(2):252–262.

Wacker L, Christl M, Synal H-A. 2010b. Bats: A new tool for AMS data reduction. Nuclear Instruments and Methods in Physics Research B 268(7):976–979.

Wacker L, Fahrni SM, Hajdas I, Molnar M, Synal H-A, Szidat S, Zhang YL. 2013. A versatile gas interface for routine radiocarbon analysis with a gas ion source. Nuclear Instruments and Methods in Physics Research B 294: 315–319.

Welte C, Wacker L, Hattendorf B, Christl M, Fohlmeister J, Breitenbach SFM, Robinson LF, Andrews AH, Freiwald A, Farmer JR, Yeman C, Synal H-A, Günther D. 2016a. Laser ablation – accelerator mass spectrometry: an approach for rapid radiocarbon analyses of carbonate archives at high spatial resolution. Anal Chem. 88(17):8570–8576.

Welte C, Wacker L, Hattendorf B, Christl M, Koch J, Synal H-A, Günther D. 2016b. Novel laser ablation sampling device for the rapid radiocarbon analysis of carbonate samples by accelerator mass spectrometry. Radiocarbon 58(2):419–435.

Welte C, Wacker L, Hattendorf B, Christl M, Koch J, Yeman C, F. M. Breitenbach S, Synal H-A, Günther D. 2017. Optimizing the analyte introduction for ^{14}C laser ablation-AMS. Journal of Analytical Atomic Spectrometry 32(9):1813–1819.

Xiaodan Z, Kaixue H, Mei L. 2016. The deconvolution algorithm of incremental wiener filtering based on pseudo-random sequences. 2016 IEEE Advanced Information Management, Communicates, Electronic and Automation Control Conference (IMCEC), Xi'an. p. 1236–1239. doi: 10.1109/IMCEC.2016.7867408.

https://doi.org/10.1017/RDC.2019.139 Published online by Cambridge University Press